Collision-Induced C₆₀ Rovibrational Relaxation Probed by State-Resolved Nonlinear Spectroscopy

Lee R. Liu,^{1,2,*} P. Bryan Changala[®],^{1,†} Marissa L. Weichman,^{1,‡} Qizhong Liang,^{1,2} Jutta Toscano[®],^{1,§} Jacek Kłos[®],³ Svetlana Kotochigova[®],³ David J. Nesbitt,^{1,2,4} and Jun Ye[®],^{1,2,¶}

¹ JILA, National Institute of Standards and Technology and University of Colorado, Boulder, Boulder, Colorado 80309, USA

Quantum state-resolved spectroscopy was recently achieved for C_{60} molecules when cooled by buffer gas collisions and probed with a midinfrared frequency comb. This rovibrational quantum state resolution for the largest molecule on record is facilitated by the remarkable symmetry and rigidity of C_{60} , which also present new opportunities and challenges to explore energy transfer between quantum states in this many-atom system. Here we combine state-specific optical pumping, buffer gas collisions, and ultrasensitive intracavity nonlinear spectroscopy to initiate and probe the rotation-vibration energy transfer and relaxation. This approach provides the first detailed characterization of C_{60} collisional energy transfer for a variety of collision partners, and determines the rotational and vibrational inelastic collision cross sections. These results compare well with our theoretical modeling of the collisions, and establish a route towards quantum state control of a new class of unprecedentedly large molecules.

DOI: 10.1103/PRXQuantum.3.030332

I. INTRODUCTION

Understanding the excitation and relaxation pathways of complex quantum mechanical systems is a primary focus of chemical and many-body physics. Precision frequency-domain spectroscopy provides a unique probe of these dynamics, elucidating structure and interactions at the level of individual molecular quantum states. High-resolution spectroscopic investigations, however, have traditionally been limited to relatively small molecules containing fewer than a dozen atoms, due to the challenges

Published by the American Physical Society under the terms of the Creative Commons Attribution 4.0 International license. Further distribution of this work must maintain attribution to the author(s) and the published article's title, journal citation, and DOI. of creating cold, controlled gas-phase samples and the intrinsic spectral congestion of larger systems.

Recently, these obstacles have been overcome for large molecules, including buckminsterfullerene C_{60} , by a combination of two key experimental techniques: (i) cryogenic buffer-gas cooling, which generates a sample of cold, gas-phase molecules, and (ii) cavity-enhanced infrared frequency comb spectroscopy, which probes the molecular rovibrational spectrum with high sensitivity and spectral resolution [1,2]. Although the initial study of C_{60} has revealed structural information, such as rotational constants, vibrational energy spacings, and the Coriolis interaction strength, the small optical power available per frequency comb component limits this approach as a fundamentally passive technique.

Further insight into the internal dynamics of large molecular systems requires the understanding and control of inherent decoherence processes. In this work, state-resolved optical pumping with a single-frequency laser reveals the existence of such processes in collisional interactions of C_{60} with atoms and diatomic molecules. Our experiments and models provide guidance for mitigating these sources of decoherence, as well as for enhancing efficiency of collisional cooling. Ultimately, we need to gain control over the internal and external degrees of freedom of individual C_{60} molecules in order to probe novel quantum dynamics with sixty interconnected C atoms.

²Department of Physics, University of Colorado, Boulder, Colorado 80309, USA

³ Department of Physics, Temple University, Philadelphia, Pennsylvania 19122, USA
⁴ Department of Chemistry, University of Colorado, Boulder, Colorado 80309, USA

⁽Received 24 May 2022; accepted 29 June 2022; published 2 September 2022)

^{*}lee.richard.liu@gmail.com

[†]Present address: Center for Astrophysics, Harvard & Smithsonian, Cambridge, MA 02138, USA.

[‡]Present address: Department of Chemistry, Princeton University, Princeton, NJ 08544, USA.

[§]Present address: Department of Chemistry, University of Basel, 4056 Basel, Switzerland.

[¶]ye@jila.colorado.edu

II. EXPERIMENTAL DETAILS

In order to manipulate rovibrational state populations and determine transition lineshapes with greatly enhanced sensitivity and precision, we demonstrate a new scheme that employs a continuous-wave (cw) laser of enhanced optical power at a specific probe frequency. Coupling a quantum cascade laser (OCL) to a high-finesse optical cavity increases the probe intensity on cold C_{60} by 10^4 fold, reaching well into the saturated absorption regime where an appreciable internal state population is driven out of thermal equilibrium. Furthermore, the concomitant 100-fold gain in sensitivity reveals detailed lineshape profiles that furnish a wealth of information on relaxation and diffusion [3-11]. We measure saturated absorption lineshape profiles and compare them to a detailed rate-equation model, thereby mapping out the propensity of C₆₀ for interconverting energy from collisions with the surrounding bath into translation and internal vibrations and rotations.

Figure 1(a) depicts the physical system under consideration. A buffer gas (BG) cooling cell is nested inside an enhancement cavity with finesse of 12 000. The cw QCL is coupled into this cavity to enhance both the intensity for nonlinear spectroscopy and detection sensitivity. Further experimental details on laser stabilization and spectroscopy scanning are provided in Appendix A. Inside the cold cell, C₆₀ collides with the surrounding BG and, as it diffuses through the cavity mode, is simultaneously pumped and probed by the intracavity field with photon

scattering rate $R_{\rm OP}$. We neglect C_{60} - C_{60} collisions because they are expected to be 6 orders of magnitude less frequent than C_{60} -BG collisions (Appendix B).

III. OPTICAL PUMPING AND COLLISION DYNAMICS

The effects on the internal state populations of the ensemble of C_{60} molecules are illustrated in Fig. 1(b). Continuous optical pumping drives the system out of thermal equilibrium, towards equal populations of the connected states and therefore a reduced absorption cross section. Simultaneously, thermal equilibrium is restored by collisions in two ways. First, inelastic collisions induce rotational and vibrational transitions at rates $\Gamma_{\rm rot}$ and $\Gamma_{\rm vib}$. Second, collisions control the rate of diffusion, which replaces optically pumped molecules in the cavity mode with thermal molecules from outside the cavity mode. In steady state, the saturation of the absorption cross section therefore provides a direct comparison between $R_{\rm OP}$ and the various rates of collisional thermalization [12].

To distinguish the effects of $\Gamma_{\rm rot}$ and $\Gamma_{\rm vib}$, we probe and compare single- and multistate pumping of C_{60} enabled by the R- and Q-branch transitions, respectively, as shown in Figs. 2(a) and 2(b). In the R branch, $\Delta J = +1$ transitions are widely spaced relative to their line width in a regular progression; therefore, only one transition is resonantly pumped at a time. Rotational relaxation from C_{60} -BG collisions redistributes pumped rotational populations into

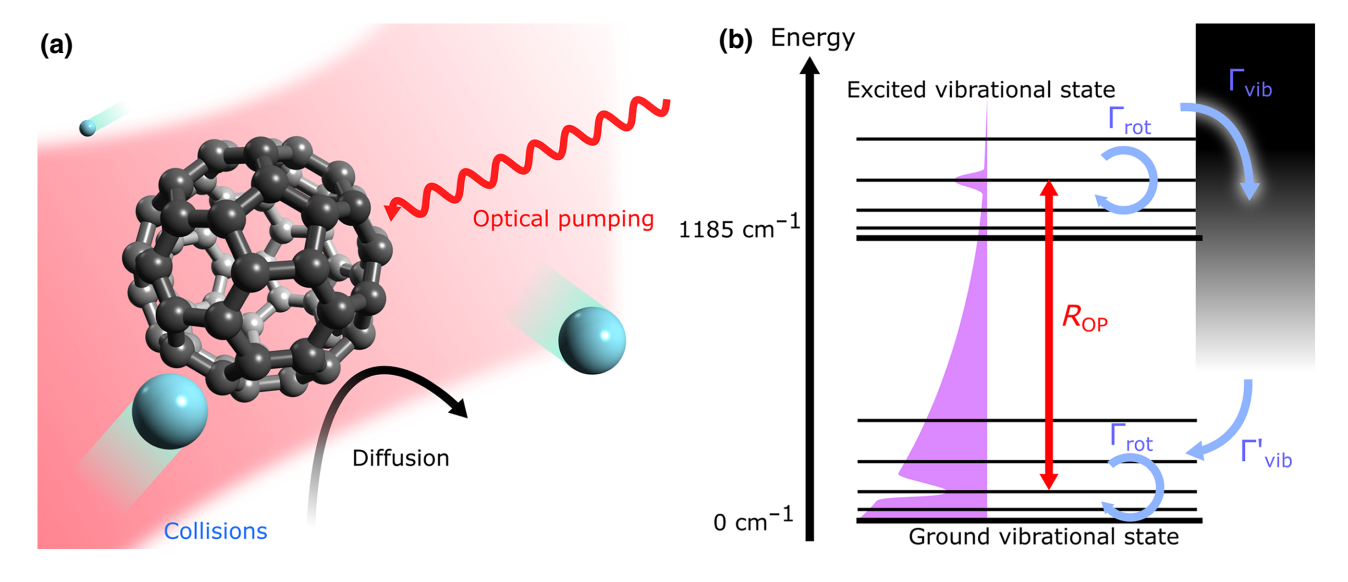


FIG. 1. Pumping and collisional relaxation processes in BG-cooled C_{60} . (a) Interactions of C_{60} with its environment. C_{60} diffuses into the optical cavity mode, where it is pumped by the cw intracavity field before diffusing out again. The experiment monitors the frequency-dependent nonlinear absorption of the intracavity field by C_{60} . Collisions with the BG control diffusion and thermalize the internal rovibrational energy of C_{60} . (b) Energy-level diagram of C_{60} undergoing interactions with the environment. Optical pumping at a rate R_{OP} drives the 1185 cm⁻¹ (8.4 μ m) $T_{1u}(3)$ vibrational band of C_{60} . Collisions with the BG redistribute rotational population at a rate Γ_{rot} , assumed to be identical in v''=0 and v'=1. Vibrational relaxation is modeled in two steps: loss of vibrational population from v'=1 into the dense reservoir of dark vibrational states at a rate Γ_{vib} , and leakage from the dense reservoir into v''=0 at a rate Γ_{vib} . Filled purple curve depicts the steady-state population distribution.

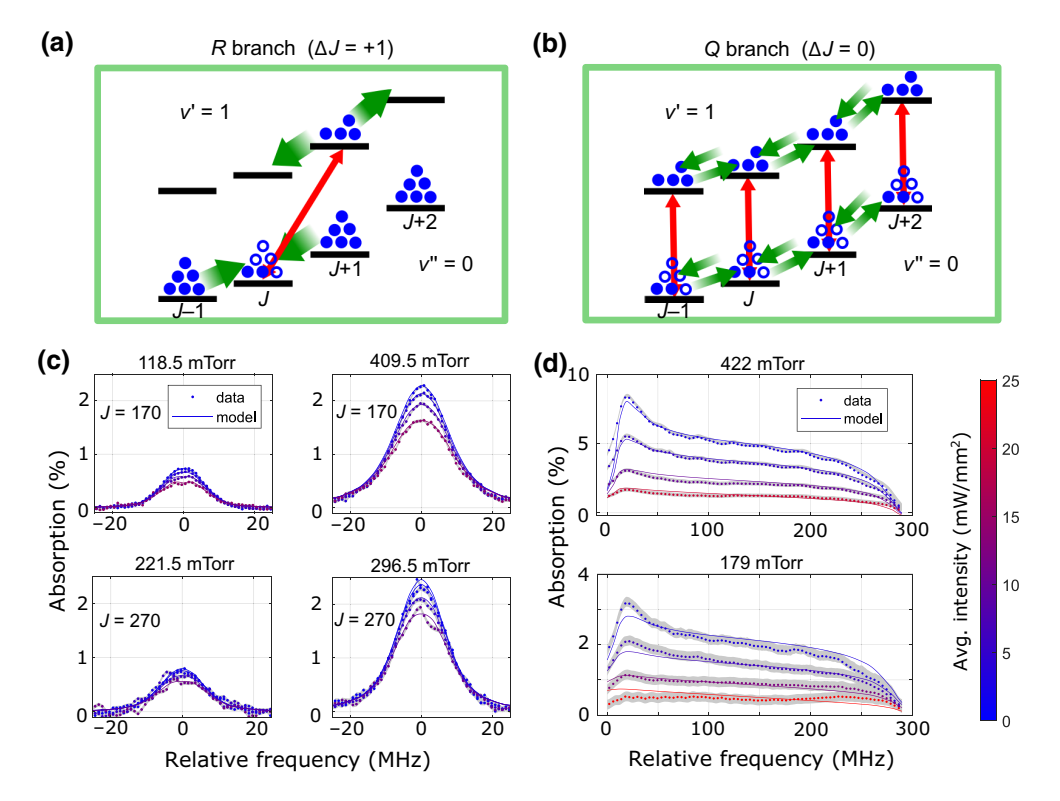


FIG. 2. Effect of single-state versus multistate pumping on rotational relaxation in C_{60} . (a) State-selective pumping in the R branch. Only a single transition can be resonantly pumped at a time; therefore, rotational relaxation from C_{60} -BG collisions efficiently redistributes pumped rotational populations (green arrows). (b) Multistate pumping in the Q branch, with many transitions (up to about 75 at the band head) being pumped simultaneously. (c) Rate equation model fits to C_{60} -Ar R-branch-saturated absorption data. Sampling of R-branch absorption data at J=170 (top) and J=270 (bottom), and corresponding rate equation fits (full C_{60} -Ar R-branch data are given in Appendix I). Good agreement is obtained by modeling state-to-state rotational relaxation with an exponential-gap law (see the text). Etalons have been fitted out and subtracted from the data. Gray bands indicate the one-sigma uncertainty in the data. (d) Rate equation model fits to C_{60} -Ar Q-branch saturated absorption data. The Q-branch absorption data and rate equation model fit (described in the text) taken at high (upper panel) and low (lower panel) Ar pressure (specified above each panel) at four pumping intensities. Only every fourth data point is plotted for clarity. Gray bands indicate standard uncertainty in the data dominated by residual etalons in the optical setup. The color of traces in panels (c) and (d) correspond to different pumping intensities, indicated by the color bar.

empty neighboring states as well as replenishes the lower state population, so that the degree of saturation measured under R-branch pumping is highly sensitive to both vibrational and rotational relaxation rates. On the other hand, the spectrally overlapping $\Delta J=0$ transitions of the Q branch permit multiple transitions to be pumped simultaneously. This renders the saturation intensity insensitive to the rotational redistribution rate, $\Gamma_{\rm rot}$. Thus, the combination of Q- and R-branch measurements allows us to distinguish between relaxation due to rotationally and vibrationally inelastic collisions.

The saturation effect is parameterized with $s_0 = i/i_{\rm sat}$, where i is the mean intracavity intensity and $i_{\rm sat}$ is the saturation intensity. We determine s_0 by measuring absorption profiles as a function of i = 2-25 mW/mm². At a typical background pressure of 300 mTorr of argon gas, this corresponds to $s_0 = 0.03-0.3$ in the R branch. Sample nonlinear spectra of the R and Q branches of C_{60} in Ar buffer gas are shown in Figs. 2(c) and 2(d), respectively. As expected,

the R branch shows a well-resolved Voigt line shape for each $\Delta J=+1$ transition, while the Q branch appears as an unresolved contour due to spectrally overlapping $\Delta J=0$ transitions. As discussed below, the Voigt profiles are dominated by homogeneous (pressure-broadening) and inhomogeneous (Doppler-broadening) widths of around 10 MHz each, while transit time broadening is expected to only be a few kilohertz. The band head in the Q branch contour arises from centrifugal distortion effects causing several $\Delta J=0$ transitions ($J''\sim 275-352$) to lie within one homogeneous linewidth of each other [2].

Notably, the Q branch is much more strongly saturated, as expected from the higher effective absorption cross section and suppression of rotational population redistribution. Since the diffusion rate (parameterized by the ensemble-averaged total cross section $\overline{\sigma}_{tot}$; see Appendix C) increases at lower pressures, while inelastic collision rates (parameterized by rotationally and vibrationally inelastic cross sections σ_{rot} and σ_{vib})

correspondingly decrease, measurement of the saturated Q- and R-branch absorption profiles over a range of BG pressures permits a complete map of energy flow from a collision to the various internal modes of C_{60} .

IV. RATE EQUATION MODEL

The foregoing discussion provides a qualitative picture of how saturated absorption measurements at suitable pressures and pumping frequencies yield $\overline{\sigma}_{tot}$, σ_{rot} , and σ_{vib} . To obtain quantitative values, we construct a rate equation model that simultaneously accounts for the evolution of states with total angular momentum J in the range 0–470 in the ground vibrational, and triply degenerate first excited vibrational states (Appendix E), enabling a least-squares fit of all frequency-dependent saturation profiles simultaneously [solid lines in Figs. 2(c) and 2(d)]. A key assumption is that the translational, rotational, and vibrational degrees of freedom of C₆₀ are completely thermalized to the BG and cell wall in the absence of optical pumping. This is supported by the fitted Doppler widths of our R-branch line shapes, rotational Boltzmann distribution observed in our previous work [2], and the good absorption contrast that indicates that C₆₀ is principally in the ground vibrational state.

We first consider isolating the rotational population dynamics by applying an exponential-gap state-to-state rotational inelastic cross-section fitting law [13–15] to a full set of J-resolved R-branch data over J=110-270 (Appendix I). We find an excellent fit across the entire range of measured J. The fitting law takes the form

$$\sigma_{\text{rot}}(J_f, J_i) = \alpha g_f e^{-\Delta E_{fi}/kT},$$
 (1)

where J_i, J_f are the initial and final J states in the same vibrational manifold, g_f is the angular momentum degeneracy of the final state calculated for the icosahedral spherical top [16], $\Delta E_{fi} = |E_f - E_i|$ is the absolute energy difference of the initial and final states, and α is a free scale parameter proportional to the thermally averaged integral cross section $\langle \sigma_{\rm rot} \rangle$:

$$\langle \sigma_{\text{rot}} \rangle \equiv \sum_{i, f \neq i} P(J_i) \sigma_{\text{rot}}(J_f, J_i)$$

$$= \alpha \sum_{i, f \neq i} P(J_i) g_f e^{-\Delta E_{fi}/kT}.$$
(2)

Here

$$P(J_i) = \frac{g_i}{Z_{\text{rot}}} \exp(-BJ_i(J_i + 1)/kT)$$
 (3)

is the normalized rotational Boltzmann weight of the initial state with rotational partition function Z_{rot} . We assume that $\sigma_{\text{rot}}(J_f, J_i)$ and therefore $\langle \sigma_{\text{rot}} \rangle$ are identical in the ground and excited vibrational states.

From the resolved R-branch lineshapes, we also extract lineshape parameters to facilitate fitting the unresolved Q branch. The R-branch lineshapes are well described by a saturated Voigt profile $f(\gamma, \sigma_D, \Delta, s_0)$ (Appendix H) parameterized by s_0 , Doppler width σ_D , laser frequency detuning Δ , and homogeneous width given by

$$\gamma \equiv n\sigma_{\rm PB}\overline{v}_{\rm rel}/\pi. \tag{4}$$

The pressure-broadening cross sections σ_{PB} provide a crucial upper limit on the total inelastic cross sections [17], as well as a proxy for dephasing in our (incoherent) rate equation model (Appendix E). Here \overline{v}_{rel} is the ensemble-averaged relative speed of the C_{60} -BG system, and takes typical values of several hundred metres per second.

Next, we consider the model for vibrational relaxation. The high vibrational density of states, about $10^2/\text{cm}^{-1}$ [18,19], for C_{60} at the energy of the 1185 cm⁻¹ excited state prompts a J-independent "reservoir model" [20, 21] for the first step of vibrational relaxation, in which $\sigma_{\text{vib}}(\text{reservoir}, J_i) = \langle \sigma_{\text{vib}} \rangle$, with the thermal average $\langle \cdot \rangle$ defined similarly as in Eq. (2). In principle, after a sufficient number of inelastic collisions, population can return to the ground vibrational state and reentre the optical cycle, with vibrational cross section $\langle \sigma'_{\text{vib}} \rangle$. Finally, diffusion causes pumped molecules to be replaced by thermalized molecules at a rate A_{diff} .

V. C₆₀-Ar COLLISION CROSS SECTIONS

Having established this physical model for C_{60} optical pumping and relaxation, we can now discuss the C_{60} -Ar collision cross sections extracted from fitting the Q- and R-branch-saturated absorption profiles. First, we set $\langle \sigma'_{\rm vib} \rangle = 0$, justified by the expectation that collisional relaxation of vibrations across the large 272 cm⁻¹ energy gap between the ground and first excited vibrational states [18] is much slower than the diffusive transport through the cavity mode. We also calculate the elastic cross section $\sigma_{\rm el}$ as a function of collision energy using a semiclassical model (Appendix D). The diffusion rate $A_{\rm diff}$ can then be obtained from

$$A_{\text{diff}} = \frac{2\overline{v}_{\text{rel}}}{n\overline{\sigma}_{\text{tot}}\chi^2_{\text{cr}}} \tag{5}$$

with (Appendix C)

$$\overline{\sigma}_{tot} = \overline{\sigma}_{el} + \langle \sigma_{rot} \rangle + \langle \sigma_{vib} \rangle. \tag{6}$$

Intuitively, x_{eff} represents the (ensemble-averaged) typical length scale over which a C_{60} molecule must diffuse in order to leave the optical pumping region.

Next, x_{eff} , $\langle \sigma_{\text{rot}} \rangle$, and $\langle \sigma_{\text{vib}} \rangle$ are varied to obtain the best simultaneous agreement of the rate equation model simulated profiles to the Q branch and R(J=170) data

as quantified by the reduced χ^2 statistic. This procedure yields $x_{\rm eff} = 0.52 \pm 0.03$ mm, $\langle \sigma_{\rm rot} \rangle = 123^{+60}_{-36} \, \mathring{\rm A}^2$, $\langle \sigma_{\rm vib} \rangle = 0.07 \pm 0.03 \, \mathring{\rm A}^2$ (uncertainties represent 68% confidence intervals). For typical operating conditions of 0.25 Torr argon, Eq. (5) then gives $A_{\rm diff} \approx 2500 \, {\rm s}^{-1}$.

VI. VARYING C₆₀ COLLISION PARTNERS

The inelastic cross sections vary as a function of the collision partner. For example, at fixed temperature and pressure, lighter BGs are expected to feature less momentum transfer per collision. Also, unlike structureless atoms, molecular rotors can exchange rotational in addition to collisional angular momentum, which can be expected to increase $\langle \sigma_{\rm rot} \rangle$. Having completed a careful characterization of C₆₀-Ar collisions, we therefore turn to the collision cross sections with other closed-shell BG species: Ne, He, D₂, and H₂. For each of these species, saturated absorption profiles of C₆₀ in the *Q* and R(J=170) branches have been measured at various BG pressures and then simultaneously fit to the rate equation model.

First, the σ_{PB} are straightforwardly obtained by fitting Voigt profiles to the resolved R-branch lineshapes and compiled in Table I. We also fix x_{eff} from the fits of the C_{60} -Ar system since it is not expected to vary with BG species. The resulting best-fit $\langle \sigma_{\rm rot} \rangle$ values for each C₆₀-BG system are plotted in Fig. 3, together with the pressure-broadening cross section σ_{PB} determined from the R-branch data, shown for reference. The complete set of fitted profiles is shown in Appendix J. Only Ar yields a measurable (>10⁻² Å²) $\langle \sigma_{\text{vib}} \rangle$, consistent with the observation that the most efficient vibrational cooling, and hence the strongest absorption signal, is obtained with the most massive collision partner [2]. Two trends are immediately apparent: (1) for rare gas atoms with no rotational structure, $\langle \sigma_{rot} \rangle$ decreases with decreasing mass, reaching a minimum for He; and (2) for diatomic BGs with a rotational degree of freedom, $\langle \sigma_{\rm rot} \rangle$ increases dramatically, despite having masses comparable to or smaller than He. The large values of $\langle \sigma_{\text{rot}} \rangle$ for C₆₀-D₂ and C₆₀-H₂ suggest that rotation-rotation energy transfer dominates [22]. Moreover, since $\langle \sigma_{\rm rot} \rangle \approx \sigma_{\rm PB}$, collisional dephasing is negligible in these two systems. These two observations are consistent with the expectation that molecular rotors can

TABLE I. Pressure-broadening cross sections σ_{PB} and the temperatures at which they are measured.

BG species	$\sigma_{ ext{PB}}\ (ext{\AA}^2)$	T(K)
Ar	430(4)	138(2)
Ne	310(4)	138(2)
Не	163(8)	159(5)
D_2	281(5)	156(3)
H ₂	243(8)	162(4)

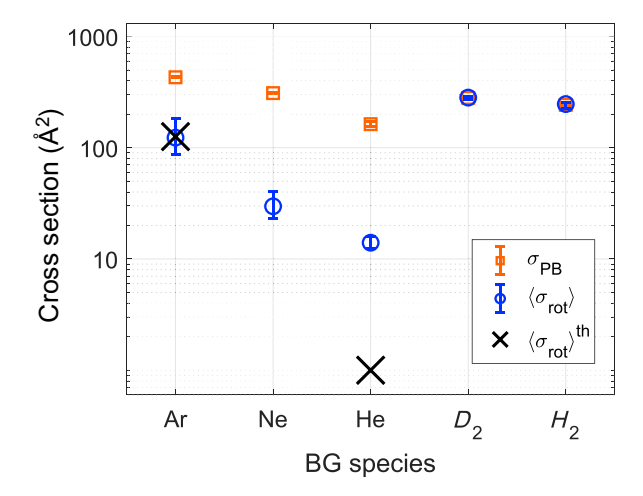


FIG. 3. Average rotational inelastic collision cross sections $\langle \sigma_{\rm rot} \rangle$ extracted from rate equation model fits to C_{60} -BG-saturated absorption data. Total pressure-broadening cross section, $\sigma_{\rm PB}$, obtained from *R*-branch fits, are plotted for reference. For rare gases with no rotational structure, $\langle \sigma_{\rm rot} \rangle$ decreases with decreasing mass, reaching a minimum for He. By comparison, the presence of a rotational degree of freedom in D_2 and H_2 results in a drastic increase of $\langle \sigma_{\rm rot} \rangle$, considering the small mass of both molecules. Error bars indicate 68% confidence intervals and include the uncertainty on the effective diffusion length $x_{\rm eff}$. Calculated values of $\langle \sigma_{\rm rot} \rangle^{\rm th}$ for C_{60} -Ar and C_{60} -He are plotted for comparison.

induce rotation-rotation relaxation from long range [23], where the interaction potential changes slowly and dephasing is less significant. By contrast, the strikingly small value of $\langle \sigma_{rot} \rangle$ for the C₆₀-He interaction suggests that this complex is very "slippery," similar to the situation observed for C₆₀-K [24].

VII. COMPARISONS WITH AB INITIO CALCULATIONS

To understand the physical origin of these results, we calculate the ground-state potential energy surface of the C_{60} -Ar and C_{60} -He complexes as functions of the position of the Ar or He atom, using ab initio density functional theory (Appendix K). We plot in Fig. 4 the potentials for C_{60} -Ar and C_{60} -He at their equilibrium bond lengths of 7.2 Å and 7.0 Å, respectively. Of the two systems, the C_{60} -He complex shows a significantly reduced potential anisotropy due to the smaller polarizability of He compared to Ar. This weak anisotropy is reflected in the small magnitude of $\langle \sigma_{\text{rot}} \rangle$ for C₆₀-He collisions. Finally, we perform accurate calculations of the various anisotropic terms in these potential energy surfaces, obtaining averaged rotationally inelastic cross sections $\langle \sigma_{\rm rot} \rangle^{\rm th} = 126 \, \text{Å}^2$ for $C_{60}\text{-Ar}$ and 1 \mathring{A}^2 for $C_{60}\text{-He}$ [25]. These are plotted alongside the experimental data in Fig. 3 for comparison. Excellent agreement is obtained for C_{60} -Ar, while C_{60} -He features a significant discrepancy. In the latter case, $\langle \sigma_{\rm rot} \rangle^{\rm th}$

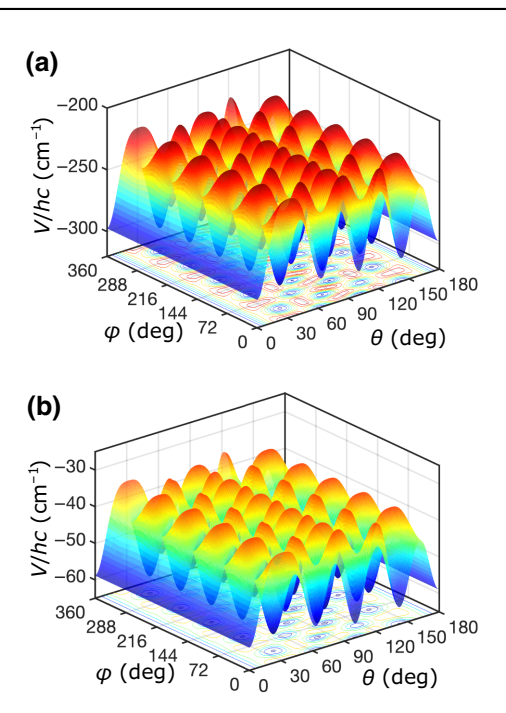


FIG. 4. Calculated potential energy surfaces for C_{60} -BG interactions. (a) Potential energy surface for C_{60} -Ar calculated at the equilibrium bond length of 7.2 Å. Polar θ and azimuthal ϕ angles are defined with respect to a Cartesian coordinate system with its x and z axes along twofold and fivefold symmetry axes of C_{60} , respectively. The potentials have minima when the Ar atom is located "above" a five- or six-membered ring of C_{60} . Local maxima occur in between the minima. The potential depth at these maxima is 20% to 30% smaller than at the minima. (b) Potential energy surface for C_{60} -He calculated at the equilibrium bond length of 7.0 Å. Note the change in vertical scale. The potential anisotropy for this complex is significantly reduced compared to that of C_{60} -Ar, and is reflected in the smaller value of its inelastic rotational cross section.

arises from the linear combination of many small terms of opposite signs in the anisotropic potential, which may lead to a large uncertainty. This suggests that our data are sufficiently precise to benchmark *ab initio* calculations of this unique collision complex.

VIII. SUMMARY

In conclusion, a simple nonlinear absorption measurement yields remarkably detailed results. Specifically, nonlinear absorption lineshapes via laser optical pumping of single R-branch transitions versus collections of rotational states in the Q branch provide pressure-broadening and rotational and vibrational inelastic collision cross sections between C_{60} and various buffer gas species. We find that $\langle \sigma_{\text{rot}} \rangle / \langle \sigma_{\text{vib}} \rangle \gtrsim 10^3$ for C_{60} -Ar around 150 K, and that $\langle \sigma_{\text{vib}} \rangle$ is not measurable at our current sensitivity for the other, less massive BGs. The small vibrational quenching cross sections are in line with C_{60} being a hard, rigid sphere [26]. The internal structure of diatomic BGs

increases $\langle \sigma_{rot} \rangle$ dramatically, likely due to rotation-rotation relaxation induced from long range. Our data are consistent with an exponential-gap law for rotational energy exchange and reveal the energy flow from the external interaction to the internal modes of C_{60} for a range of collision partners. We find excellent agreement of C_{60} -Ar rotational inelastic cross sections with *ab initio* calculations.

Our experiments and calculations motivate and benchmark future theoretical work, and open a new avenue for probing collisional relaxation dynamics of an unprecedentedly large and symmetric molecule. Specific and precise state-to-state cross sections could be determined in future experiments where the effect of a cw optical pump is probed with a frequency comb across all relevant rotational states simultaneously.

ACKNOWLEDGMENTS

The authors thank D. Rosenberg and T. Q. Bui for technical assistance and discussions. This research is supported by AFOSR Grant No. FA9550-19-1-0148, the National Science Foundation Quantum Leap Challenge Institutes Office of Multidisciplinary Activities (Grant No. 2016244); the National Science Foundation (Grant No. Phys-1734006); the Department of Energy (DE-FG02-09ER16021); and the National Institute of Standards and Technology. J.T. is supported by a Lindemann Trust Post-doctoral Fellowship. J.K. and S.K. acknowledge support from the U.S. AFOSR under Grant No. FA9550-21-1-0153 and the NSF under Grant No. PHY-1908634.

APPENDIX A: EXPERIMENTAL DETAILS

The high-finesse spectroscopy cavity (finesse $F = 12\,000$; Gaussian beam waist $w_0 = 1.1$ mm) intersects a $6 \times 6 \times 6$ cm³ aluminum cold cell held between 130–160 K. C₆₀ evaporates from an oven and is entrained in a flow of BG into the cell, where it thermalizes to the BG and cell temperature [2].

The optical beam path is shown in Fig. 5. The light is derived from an Alpes Lasers cw QCL powered by a home-built current driver. To narrow down the 20 MHz free-running linewidth for efficient coupling into the spectroscopy cavity, half of the beam power is picked off and frequency locked to an external three-mirror V-shaped reference cavity machined out of a single block of aluminum and purged with N_2 gas (free spectral range of 725 MHz). The cavity length can be tuned over twice the free spectral range by a ring piezo mounted to the cavity spacer. Only light resonant with the cavity is reflected back to the QCL, providing reduction of the laser linewidth via optical feedback stabilization [28–30]. While the relative laser-reference cavity linewidth is estimated to be < 1 kHz, jitter of the reference cavity itself widens the absolute

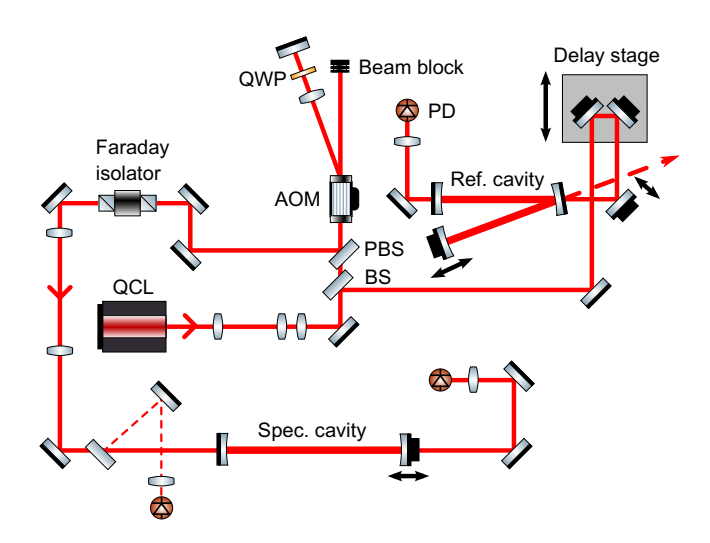


FIG. 5. Optical beam path for the experiment. The $8.4~\mu m$ beam from the QCL is split into two paths by a beam splitter (BS). (1) The reflected beam is locked to a reference cavity that provides optical feedback to narrow the laser linewidth (see the text). To enable optical feedback stabilization, a delay stage and bullet mount piezo mirror [27] provide slow and fast control of the round-trip optical phase, while a piezo-mounted cavity mirror stretches the reference cavity length. (2) The transmitted beam is PDH locked to the spectroscopy cavity, with a double-pass AOM and piezo-mounted cavity mirror for the fast and slow frequency feedback, respectively. The absorption signal is monitored by a photodiode on the cavity transmitted output. Double-sided arrows depict the direction of travel of the mirrors. PBS, polarizing beam splitter; QWP, quarter waveplate; PD, photodetector.

laser linewidth to \lesssim 10 kHz. The cavity frequency is passively stable to within a few parts per million (ppm) (a few kilohertz) over an hour, whereas the optical feedback stabilization locking bandwidth is 200 MHz. However, the laser-cavity round-trip optical phase requires active stabilization due to the path length of about 1 m. We dither the free-running laser frequency by applying a 100 kHz sinewave on top of the QCL drive current and demodulate the reference cavity transmitted intensity to produce an error signal for the round-trip phase. This is fed back to the delay stage and bullet-mounted piezo mirror that provide slow and fast control, respectively, of the path length to maintain optimal conditions for optical feedback stabilization. To scan the optical frequency of the reference cavity mode, the cavity length and round-trip phase are tuned simultaneously. The stabilized QCL beam is locked to the spectroscopy cavity using a Pound-Drever-Hall (PDH) lock, with a piezo-mounted cavity mirror and double-pass acousto-optic modulator (AOM) providing slow and fast frequency control, respectively.

To obtain an absorption spectrum, the spectroscopy and reference cavity lengths and path length delay are scanned simultaneously with the cw-QCL current back and forth over a frequency range of 500–600 MHz over a 4-s period, while the transmission through the spectroscopy cavity is monitored with a liquid-nitrogen cooled detector (Kolmar KLD-0.5-J1/11/DC). A separate 1064-nm laser (Coherent Mephisto) reflected off the reference cavity scanning mirror monitors the relative frequency excursion by counting interference fringes.

To determine the cell pressure, a long $\frac{1}{4}$ -in. diameter stainless steel bellows is attached to the cold cell, and the other end to a capacitance manometer thermally anchored to the chamber wall at room temperature. The zero-flow condition ensures that the pressure measurement is consistent with that at the cold cell, while the capacitance manometer operates at room temperature. We assume that the pressure is essentially that of the BG alone, as the concentration of C_{60} is estimated at the ppm level (Appendix B). The cold cell temperature is measured with a thermocouple attached to the cell wall. Pressure in the cold cell can be varied from 100–500 mTorr by choking the pumping speed and varying the BG flow rate.

The intracavity power is obtained by dividing transmitted power by the mirror transmission of 200 ppm, independently verified by cavity finesse and transmission measurements. The intensity is obtained by dividing by πw_0^2 , where $w_0 = 1.1$ mm is the Gaussian beam waist obtained from ABCD calculations.

Residual etalon fringes in our optical setup have a period of about 200 MHz. Since this is much larger than the linewidth of the resolved *R*-branch peaks, etaloning can be removed by fitting to a suitable lineshape function (Appendix H). However, the *Q*-branch contour spans about 270 MHz, completely masking the etalon fringes and making them a dangerous source of systematics. We carefully tilt and isolate optical surfaces to suppress the intensity fluctuations due to etalons down to about 0.2%. These residual uncertainties are included in the *Q*-branch data as gray error bands.

APPENDIX B: EFFECT OF C₆₀-C₆₀ COLLISIONS

Here we estimate the C_{60} - C_{60} collision rate. First, we estimate the number density at typical operating conditions of 150 K and 300 mTorr buffer gas pressure. The integrated Napierian absorbance of the unsaturated Q branch is measured to be $\int \ln(I_0/I(\nu))d\nu = 9 \times 10^{-4} \text{ cm}^{-1}$. The total band absorbance for all C_{60} isotopologues is therefore estimated to be

$$A = 3 \frac{1}{0.51} \int \ln \left(\frac{I_0}{I(\nu)} \right) d\nu = 5.3 \times 10^{-3} \text{ cm}^{-1}.$$
 (B1)

The factor of 3 is because the Q branch accounts for only one-third of the total vibrational band strength, and the factor of 1/0.51 is because $^{12}C_{60}$ only accounts for 51% of all C_{60} isotopologues [31].

TABLE II. Estimate of the relative C_{60} - C_{60} collision rate.

Parameter	C_{60} - C_{60} : C_{60} -BG	
n	$1/(6 \times 10^5)$	
$\overline{\sigma}_{ ext{tot}}$	4	
$\overline{v}_{ m rel}$	1/13 (H ₂)–1/3 (Ar)	
$\Gamma_{\rm tot} = n\overline{\sigma}_{\rm tot}\overline{v}_{\rm rel}$	$5 \times 10^{-7} - 2 \times 10^{-6}$	

From the molar absorptivity $\Psi = \ln(10) \times 9.9$ km/mol [32], cavity finesse $F = 12\,000$, and buffer gas cell length l = 6 cm, we can estimate the number density in the cell as

$$n = \frac{A}{2\Psi F l/\pi} = 5 \times 10^{-11} \text{ mol/L}.$$
 (B2)

Note that this provides an underestimate of the C_{60} - C_{60} collision rate since it is only based on the measured absorbance from the cold, ground vibrational state C_{60} . By contrast, at 300 mTorr and 150 K, the buffer gas number density is 3×10^{-5} mol/L, 6×10^{5} higher than that calculated for C_{60} . The total collision rate is therefore expected to be between $(0.5–2) \times 10^{-6}$ times less for C_{60} - C_{60} collisions than for C_{60} -BG collisions (Table II). The minimum inelastic cross sections we can measure are of the order $10^{-5} \times \overline{\sigma}_{tot}$. Hence, even in the extreme case $\sigma_{inel} = \overline{\sigma}_{tot}$ for C_{60} - C_{60} collisions, relaxation from C_{60} - C_{60} collisions would not be detected by our experiment, and we ignore them in this work.

APPENDIX C: LANGEVIN DIFFUSION CONSTANT

The drag force from C_{60} colliding with BG atoms is given by

$$\langle F \rangle_t = -\alpha \langle v \rangle_t$$

$$= \langle \Delta p \rangle_t / \tau$$

$$= -2\mu \langle v \rangle_t / \tau, \qquad (C1)$$

where α is the drag force coefficient, $\langle v \rangle_t$ is the speed of C_{60} , $\langle \Delta p \rangle_t$ is the momentum change experienced by C_{60} per collision, τ is the mean time between C_{60} -BG collisions, and μ is the reduced mass of the C_{60} -BG system. The symbol $\langle \cdot \rangle_t$ is the "long-time average," where the averaging time is large compared to τ . Therefore, the drag force coefficient is given by

$$\alpha = 2\mu/\tau. \tag{C2}$$

The spatial diffusion coefficient is given by [33–35]

$$D = \frac{kT}{\alpha} = kT \frac{\tau}{2\mu} = \frac{1}{2} \frac{\overline{v}_{\text{rel}}}{n\overline{\sigma}_{\text{tof}}},$$
 (C3)

where n is the number density of the buffer gas, $\overline{v}_{\rm rel}$ is the ensemble-averaged relative speed of the C₆₀-BG system, and $\overline{\sigma}_{\rm tot} = \sigma_{\rm el}(\overline{v}_{\rm rel}) + \langle \sigma_{\rm rot} \rangle + \langle \sigma_{\rm vib} \rangle$ is approximately the thermal and J-averaged total cross section. Here we are implicitly making the approximation for the elastic collision rate constant $\overline{\sigma_{\rm el}v_{\rm rel}} \approx \sigma_{\rm el}(\overline{v}_{\rm rel})\overline{v}_{\rm rel}$, which has an error of about 2% for our temperatures of interest. Elastic cross sections $\sigma_{\rm el}$ as a function of collision energy are calculated in Appendix D.

The diffusion time t_{diff} , mean squared distance $\langle \Delta x^2 \rangle$, and diffusion coefficient D are related by

$$2NDt_{\text{diff}} = \langle \Delta x^2 \rangle, \tag{C4}$$

where N is the dimensionality [33]. Here, N=2 because we are only sensitive to diffusion in the two spatial dimensions transverse to the cavity mode (which is very nearly collimated). Setting the diffusion rate $A_{\text{diff}} = (t_{\text{diff}})^{-1}$ and the effective diffusion length $x_{\text{eff}} = \sqrt{\langle \Delta x^2 \rangle}$ yields

$$A_{\text{diff}} = \frac{2\overline{v}_{\text{rel}}}{n\overline{\sigma}_{\text{tot}}x_{\text{eff}}^2}.$$
 (C5)

APPENDIX D: CALCULATING ELASTIC CROSS SECTIONS

We first estimate the long-range van der Waals dispersion coefficient C_6 for the C_{60} -BG systems. First, we calculate the dynamic dipole polarizability tensor $\alpha_{ij}(\omega)$ with i,j=x,y, and z as a function of the imaginary-valued frequency ω for rigid C_{60} using the coupled-cluster propagator with single and double excitations and the STO-3G basis set in Molpro [36]. The body-fixed coordinate system (x,y,z) is defined as in Fig. 4 of the main text. The basis set in this calculation, however, is not sufficiently accurate. We therefore also calculate the static, $\omega=0$ dipole polarizability tensor in Q-Chem [37] with the much-larger 6-311G(d,p) basis and the functionals of Refs. [38,39].

These accurate values of the static dipole polarizability tensor are shown in Table III. The corresponding isotropic static polarizability of C_{60} is $\alpha_{iso}(0) = \sum_i \alpha_{ii}(0)/3 = 502.6 \ a_0^3$ or 74.54 Å³, where a_0 is the Bohr radius, and agrees well with the measured static polarizability of 79 \pm 4 Å³ [40]. The anisotropic components of $\alpha_{ij}(0)$ are 6 orders of magnitude smaller. Finally, we uniformly scale the coupled-cluster calculations of the dynamic dipole

TABLE III. Static dipole polarizability tensor elements α_{ij} (0) of C₆₀ in units of a_0^3 .

	X	У	Z
<u></u>	502.6413	0.0000	0.012 62
y	0.0000	502.6394	0.0000
Z	0.01262	0.0000	502.6453

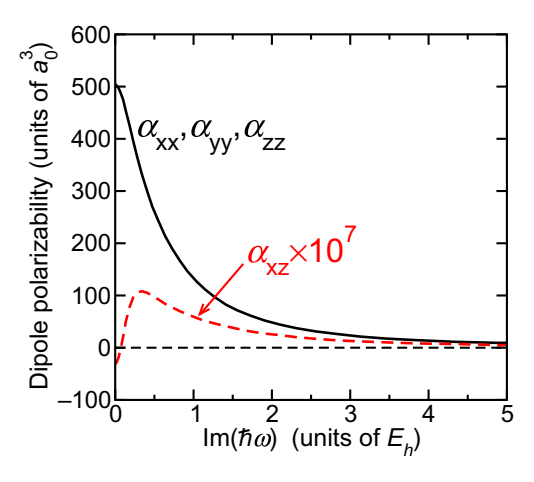


FIG. 6. Our calculated dipole polarizability tensor elements of C_{60} as functions of imaginary frequency $Im(\omega)$. The off-diagonal tensor elements have been multiplied by 10^7 for clarity.

polarizability tensor such that its isotropic static dipole polarizability coincides with that from the Q-Chem calculation. The resulting dipole polarizability tensor elements as a function of the imaginary frequency are shown in Fig. 6.

By combining our frequency-dependent polarizability tensor of C_{60} and the frequency-dependent dipole polarizability of the noble gas atoms from Ref. [41] in the Casimir-Polder formula, we find the isotropic C_6 coefficients listed in Table IV. Here, E_h is the Hartree energy. We are in reasonable agreement with the 2035 $E_h a_0^6$ value for C_{60} -Ar from Ref. [42]. Since we only consider electronic contribution to the polarizability, the C_6 coefficients for C_{60} -D₂ and C_{60} -H₂ are identical.

Finally, the elastic cross sections as a function of the relative collision velocity $v_{\rm rel}$ in the approximation of high-energy phase shift and R^{-6} long-range potential can be computed from [43,44]

$$\sigma_{\rm el} = 8.083 \left(\frac{C_6}{\hbar v_{\rm rel}}\right)^{2/5}.\tag{D1}$$

These are plotted in Fig. 7 for all BG species considered in this work.

TABLE IV. The C_6 coefficients of C_{60} -BG in units of $E_h a_0^6$.

	$C_6 (E_h a_0^6)$
C ₆₀ -He	369.544 52
C ₆₀ -Ne	749.396 67
C ₆₀ -Ar	2523.003 69
C_{60} - D_2 , H_2	1094.615 95

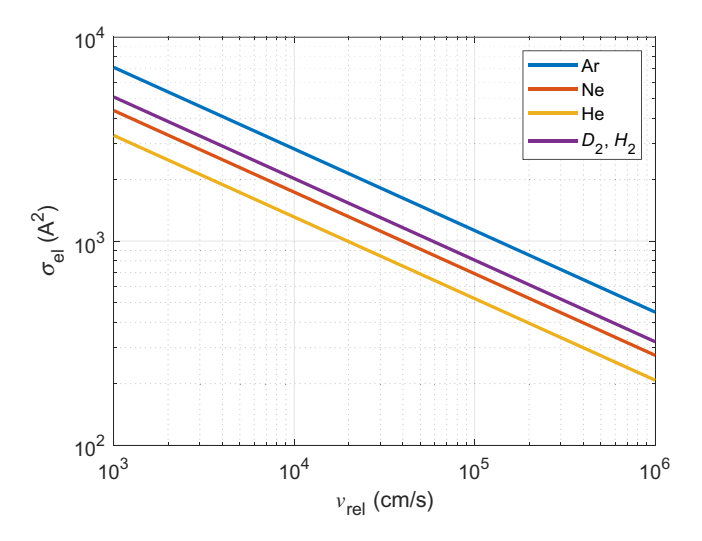


FIG. 7. Our calculated semiclassical elastic cross sections σ_{el} as functions of the relative collision velocity v_{rel} .

APPENDIX E: RATE EQUATION MODEL

The small rotational constant, rapidly increasing vibrational density of states with energy, and the thousands of accessible rotational states even at cryogenic temperatures render the full theoretical description of collisional relaxation dynamics a formidable task. We turn to a rate equation model to extract the most salient physics, the partitioning of collisional energy into inelastic vibrational and rotational transitions.

In our cw spectroscopy scans, the maximum frequency slew rate is $400 \text{ MHz/s} \approx 40 \times \gamma/\text{s}$. The 1/40 s timescale is by far the longest timescale among the mean time between collisions ($\lesssim 10^{-7} \text{ s}$) or diffusion-limited beam transit time ($\lesssim 10^{-3} \text{ s}$). Also, the translational and rotational degrees of freedom are assumed to be completely thermalized to the BG and cell wall. This is supported by the rotational Boltzmann spectrum observed in our previous work [2].

We therefore assume that the probed system is always in steady state. Calculating the absorption cross section then amounts to finding the steady-state rovibrational populations in the presence of optical pumping, collisions, and diffusion. We solve a steady-state rate equation of the form

$$\frac{d}{dt}\mathbf{v}_0 = (\mathbf{K} + \mathbf{R})\mathbf{v}_0 = 0, \tag{E1}$$

where \mathbf{v}_0 is the vector containing steady-state populations of every rovibrational state under consideration. Here \mathbf{K} is the transition rate matrix for all thermal (i.e., collision and diffusion) processes and \mathbf{R} is that for optical pumping. In block-matrix form $(\mathbf{K} + \mathbf{R})\mathbf{v}_0$ is

$$\left(\begin{array}{c|cccc}
v = 0 & v = 0 \leftarrow v = 1 & v = 0 \leftarrow \text{res} \\
\hline
v = 0 \rightarrow v = 1 & v = 1 & v = 1 \leftarrow \text{res} \\
\hline
v = 0 \rightarrow \text{res} & v = 1 \rightarrow \text{res} & \text{res}
\end{array}\right)
\left(\begin{array}{c}
\mathbf{N}_{0} \\
\mathbf{N}_{1} \\
\mathbf{N}_{res},
\end{array}\right), (E2)$$

where

$$\mathbf{N}_0 = \left(P_{v=0}^J(J=0), P_{v=0}^J(J=1), \dots, P_{v=0}^J(J=J_{\text{end}})\right)$$
(E3)

is the $N_0 \times 1$ vector of populations of each J state in the v = 0 manifold (where $N_0 = J_{\text{end}} + 1$),

$$\mathbf{N}_{1} = \left(P_{v=1}^{J+1}(J=0), P_{v=1}^{J+1}(J=1), \dots, P_{v=1}^{J+1}(J=J_{\text{end}}), P_{v=1}^{J}(J=0), P_{v=1}^{J}(J=1), \dots, P_{v=1}^{J}(J=J_{\text{end}}), P_{v=1}^{J-1}(J=0), P_{v=1}^{J-1}(J=1), \dots, P_{v=1}^{J-1}(J=J_{\text{end}})\right)$$
(E4)

is the $N_1 \times 1$ vector of populations of each J state in the v = 1 manifold [where $N_1 = 3 \times (J_{\text{end}} + 1)$], and N_{res} is the 1×1 entry corresponding to the total population residing in the dark vibrational reservoir. Here, $P_{\nu}^{R}(J)$ denotes the population in the quantum state $|R, J, v\rangle$, where the "pure rotational" angular momentum quantum number R arises from the coupling of J to the vibrational angular momentum due to Coriolis forces [2]. In the v = 1 vibrational excited state, R = J, $|J \pm 1|$, thereby sorting the excited state into three Coriolis manifolds. We account for J up to $J_{\text{end}} = 470$. We have assumed that the lab-fixed and body-fixed projections, m and k, respectively, are mixed infinitely quickly, which corresponds to instantaneous and uniform reorientation of the C_{60} molecule. The steady-state solution equals the zero-eigenvalue eigenvector of the total transition rate matrix $\mathbf{K} + \mathbf{R}$, which yields the steady state N_0 , N_1 , and N_{res} .

The relaxation matrix K is the sum of rate matrices for all thermal processes: rotationally inelastic collisions, vibrationally inelastic collisions, diffusion of molecules out of the optical pumping beam, spontaneous emission, and blackbody pumping,

$$\mathbf{K} = n\overline{v}_{\text{rel}}(\mathbf{K}_R + \mathbf{K}_V) + A_{\text{diff}}\mathbf{K}_D + \mathbf{K}_{\text{SE}}$$
 (E5)

with the diffusion rate A_{diff} derived in Appendix C. The rotational relaxation matrix \mathbf{K}_R only couples J states

within a vibrational state, i.e.,

$$\mathbf{K}_{R} = \sigma_{\text{rot}} \begin{pmatrix} \mathbf{K}_{R}^{(1)} & 0 & \vdots \\ & 0 & \vdots \\ & & 0 \\ \hline & & 0 \\ 0 & \mathbf{K}_{R}^{(2)} & \vdots \\ & & 0 \\ \hline 0 \cdots 0 & 0 \cdots 0 & 0 \end{pmatrix}. \quad (E6)$$

The upper triangle, not including the main diagonal, corresponds to downward transitions (i.e., that decrease rotational energy),

$$\{\mathbf{K}_{R}^{(1)}\}_{f,i>f} = g_f \exp(-\Delta E_{f,i}/kT),$$
 (E7)

where f, i index the final and initial states, respectively, and g_f and $\Delta E_{f,i}$ are defined in the main text. By detailed balance, the lower triangle is given by

$$\{\mathbf{K}_{R}^{(1)}\}_{f,i< f} = \frac{g_f}{g_i} e^{-(E_f - E_i)/kT} \{(\mathbf{K}_{R}^{(1)})^{\mathsf{T}}\}_{f,i< f}.$$
 (E8)

Finally, to conserve population, the diagonal elements $\{\mathbf{K}_{R}^{(1)}\}_{f,i=f}$ are chosen to make the columns sum to zero.

We have assumed that the different Coriolis manifolds are uncoupled by rotational relaxation. Hence, $\mathbf{K}_{R}^{(2)}$ is block diagonal:

$$\mathbf{K}_{R}^{(2)} = \begin{pmatrix} \mathbf{K}_{R(l=-1)}^{(2)} & 0 & 0 \\ & & & & \\ \hline & 0 & \mathbf{K}_{R(l=0)}^{(2)} & 0 \\ & & & & \\ \hline & 0 & 0 & \mathbf{K}_{R(l=+1)}^{(2)} \end{pmatrix}$$
(E9)

with the $\mathbf{K}_{R(l=-1,0,+1)}^{(2)}$ matrices each defined similarly to $\mathbf{K}_{R}^{(1)}$.

The vibrational relaxation matrix \mathbf{K}_V couples the vibrational manifolds to the vibrational reservoir. Direct $v=1 \leftrightarrow v=0$ transitions due to inelastic collisions are neglected:

$$\mathbf{K}_{V} = \begin{pmatrix} \mathbf{D}^{(1)} & 0 & \mathbf{K}_{V}^{(0 \leftarrow \text{res})} \\ \hline 0 & \mathbf{D}^{(2)} & \mathbf{K}_{V}^{(1 \leftarrow \text{res})} \\ \hline \mathbf{K}_{V}^{(0 \rightarrow \text{res})} & \mathbf{K}_{V}^{(1 \rightarrow \text{res})} & \mathbf{D}^{(3)} \end{pmatrix}$$
(E10)

with

$$\mathbf{K}_{V}^{(1 \to \text{res})} = \sigma_{\text{vib}}(1, 1, \dots, 1), \tag{E11}$$

$$\mathbf{K}_{V}^{(1 \leftarrow \text{res})} = (\mathbf{K}_{V}^{(1 \to \text{res})})^{\intercal} \odot \left(\frac{Z_{v=1}}{Z_{\text{res}}} \times \left(\mathbf{P}_{f}' / \sum_{f} P_{f}'\right)\right), \tag{E12}$$

$$\mathbf{K}_{V}^{(0\to \text{res})} = \sigma'_{\text{vib}}(1, 1, \dots, 1),$$
 (E13)

$$\mathbf{K}_{V}^{(0 \leftarrow \text{res})} = (\mathbf{K}_{V}^{(0 \rightarrow \text{res})})^{\mathsf{T}} \odot \left(\frac{Z_{v=0}}{Z_{\text{res}}} \times \left(\mathbf{P}_{f}^{"} / \sum_{f} P_{f}^{"} \right) \right). \tag{E14}$$

Here "O" denotes elementwise multiplication and the matrices of Maxwell-Boltzmann probability weights are given by

$$\mathbf{P}''_{f} = \{g_{f} \times e^{-E_{f}/kT}\}_{f}, \quad f = 1, 2, \dots, N_{0},$$

$$\mathbf{P}'_{f} = \{g_{f} \times e^{-E_{f}/kT}\}_{f}, \quad f = N_{0} + 1, N_{0}$$

$$+ 2, \dots, N_{0} + N_{1},$$
(E16)

with f denoting the final state index. Vibrational partition functions $Z_{\nu=0}$, $Z_{\nu=1}$, $Z_{\rm res}$ are calculated in Appendix F. The block matrices on the main diagonal, $\mathbf{D}^{(1)}$, $\mathbf{D}^{(2)}$, and $\mathbf{D}^{(3)}$, are diagonal matrices, whose elements are set by making the columns of \mathbf{K}_V sum to zero, as before.

The diffusion matrix \mathbf{K}_D is constructed by filling each column with the Boltzmann probability weights of the final state:

$$\frac{1}{Z_{\text{vib}}} \left((Z_{v=0} + Z_{v=1}) \mathbf{P}_f / \sum_f P_f, Z_{\text{res}} \right)^{\mathsf{T}}$$
 (E17)

with $Z_{\text{vib}} = Z_{v=0} + Z_{v=1} + Z_{\text{res}}$ and the Boltzmann weights given by

$$\mathbf{P}_f = \{g_f \times e^{-E_f/kT}\}_f, \quad f = 1, 2, \dots, N_0 + N_1.$$
 (E18)

Then, the diagonals of \mathbf{K}_D are adjusted to make the columns sum to zero. Thus, any molecule leaving the

pumping volume is replaced by a molecule drawn from the Boltzmann distribution.

Blackbody pumping and stimulated emission are described by the matrix $\mathbf{K}_{\rm SE}$. For the spherical top, blackbody radiation and spontaneous emission couple states in $v=1 \leftrightarrow v=0$ with identical R quantum number (we do not consider any radiative coupling with the vibrational reservoir). The upper triangular (i.e., downward transition) matrix elements contain terms for emission stimulated by blackbody radiation and spontaneous emission. Here, $A_{21}^v=1.4~{\rm s}^{-1}$ [45] is the vibrational Einstein A coefficient, calculated using an integrated band strength of 24 km mol $^{-1}$ from KBr matrix measurements [32]. The total thermal radiative decay rate $B_{21}^v\rho(v)+A_{21}^v\approx A_{21}^v$ since, at $T=150~{\rm K}$ and $v/c=1185~{\rm cm}^{-1}$ [12],

$$B_{21}^{\nu}\rho(\nu) = A_{21}^{\nu}/(\exp(h\nu/kT) - 1)$$

$$= \frac{A_{21}^{\nu}}{8.5 \times 10^4}.$$
(E19)

Furthermore, the probed vibrational bandwidth is less than 7 cm⁻¹. The variation in the A constant (which scales as v^3) is only 2% across this entire range, so we assume it to be J independent.

With these approximations, we now define upper triangular matrix elements of \mathbf{K}_{SE} :

$$\{\mathbf{K}_{\text{SE}}\}_{f,i>f} = \begin{cases} A_{21}^{v}, & R_i = R_f \text{ (dipole selection rule),} \\ 0, & \text{otherwise.} \end{cases}$$
(E20)

The lower triangular matrix elements are determined by detailed balance, i.e.,

$$\{\mathbf{K}_{SE}\}_{f,i < f} = \frac{g_f}{g_i} e^{-(E_f - E_i)/kT} \{(\mathbf{K}_{SE})^{\mathsf{T}}\}_{f,i < f}.$$
 (E21)

Then the diagonals are again chosen to make the columns sum to zero.

The pumping matrix accounts for homogeneous collisional (dephasing and lifetime) and inhomogeneous (Doppler) broadening and pumping from counterpropagating beams. We first consider pumping of a single velocity class with Doppler shift δ in the lab frame, with the pump laser frequency at v_I .

Off-diagonal matrix elements of \mathbf{R}_{OP} are given by the photon absorption and stimulated emission rates:

$$\{\mathbf{R}_{\mathrm{OP}}\}_{f,i} = \begin{cases} \frac{I\sigma_a(\nu_l)}{h\nu_l}, & i > f \text{ (upper triangle),} \\ \frac{I\sigma_{\mathrm{SE}}(\nu_l)}{h\nu_l}, & i < f \text{ (lower triangle).} \end{cases}$$
(E22)

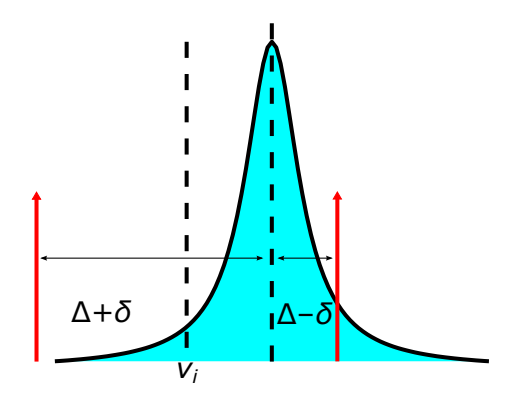


FIG. 8. Pumping of a single velocity class (Doppler shifted to $v_i + \delta$) by counterpropagating beams with lab-frame detuning Δ .

Here I is the intensity, and the absorption and stimulated emission cross sections are [12]

$$\sigma_{a}(\nu_{l}) = \sum_{k} \left(\frac{2J_{k}'+1}{2J_{k}''+1}\right) \frac{\lambda_{k}^{2}}{8\pi} A_{21}^{\nu}$$

$$\frac{L(\Delta_{k}+\delta,\gamma) + L(\Delta_{k}-\delta,\gamma)}{2}, \qquad (E23)$$

$$\sigma_{SE}(\nu_l) = \sum_{k} \frac{\lambda_k^2}{8\pi} A_{21}^{\nu} \frac{L(\Delta_k + \delta, \gamma) + L(\Delta_k - \delta, \gamma)}{2},$$
(E24)

which ensures that the pumping of each transition individually satisfies detailed balance. The sum over k runs over all dipole-allowed transitions (with selection rule $R_i = R_f$), and the sum of two detuned Lorentzians account for pumping from two counterpropagating beams (Fig. 8). The line shape function,

$$L(x, \gamma) = \frac{\gamma}{2\pi} \frac{1}{x^2 + (\gamma/2)^2},$$
 (E25)

is an area-normalized Lorentzian. By $\Delta_k = \nu_l - \nu_k$ we denote the detuning from the *rest-frame* molecular resonance frequency of the *k*th transition; $\lambda_k = c/\nu_k$ is the wavelength of the *k*th transition. Expressions for ν_k are given in Appendix G. No optical pumping of states in the vibrational reservoir is considered since those transitions will be far off resonance.

Finally, to conserve probability, the diagonals of \mathbf{R}_{OP} are set to make the sum of columns zero.

We have accounted for dephasing and lifetime broadening by manually incorporating an area-normalized, pressure-broadened homogeneous linewidth γ for the frequency-dependent absorption cross section. Thus, the direct effect of homogeneous broadening on the effective pumping rate is to depress the peak absorption cross

section on resonance and spread it to neighboring frequencies. This model ignores coherences in collision- or diffusion-induced population transfer, and assumes that the radiation field only drives pairs of states at a time without inducing coherences between three or more levels.

To account for inhomogeneous broadening, we discretize the Doppler velocity profile $P(v_z) = g(\gamma = 0, \sigma_D, \beta = 0, v_z/\lambda)$ [lineshape function g is defined in Eq. (H1)] into bins, each spanning from v_z to $v_z + dv_z(v_z)$. The $dv_z(v_z)$ are calculated to give constant partial integrated probability (made sufficiently small to give convergence in profile fitting)

$$P(v_z)dv_z(v_z) = \begin{cases} 0.1, & Q \text{ branch,} \\ 0.03, & R \text{ branch.} \end{cases}$$
 (E26)

For each bin, we solve for the velocity-class-resolved partial equilibrium population distributions $\mathbf{v}_0^{v_z}$ with $\delta = v_z/\lambda$. Their weighted sum yields the total population distribution

$$\sum_{v_z} P(v_z) dv_z(v_z) \times \mathbf{v}_0^{v_z} = \mathbf{v}_0^{\text{tot}}.$$
 (E27)

This sum assumes that velocity classes are totally decoupled, a conclusion that is independently supported by the R-branch lineshape fitting (Appendix H). Finally, the full absorption spectrum is obtained by repeating this calculation for different values of the laser frequency v_l .

APPENDIX F: VIBRATIONAL PARTITION FUNCTIONS

We calculate the vibrational partition functions for detailed balancing of the vibrational state transition matrix [Eq. (E10)]. We assume a temperature of 150 K. The total partition function of C_{60} vibrational modes i, with degeneracy g_i and vibrational energy spacing $\hbar \omega_i$, is

$$Z_{\text{vib}} = \prod_{i} (Z_{1D}^{i})^{g_{i}}$$

$$= \prod_{i} \frac{1}{(1 - e^{-\hbar\omega_{i}/kT})g_{i}}$$

$$= 2.74.$$
 (F1)

The contributions to the partition function from the ground state and excited triply degenerate 1185 cm⁻¹ $T_{1u}(3)$ state

$$Z_{v=0} = 1, (F2)$$

$$Z_{v=1} = 3 \times e^{-1185 \text{ cm}^{-1}/kT} = 4 \times 10^{-5}.$$
 (F3)

The partition function of the reservoir is therefore approximately

$$Z_{\text{res}} \approx Z_{\text{vib}} - Z_{\nu=0} - Z_{\nu=1} = 1.74.$$
 (F4)

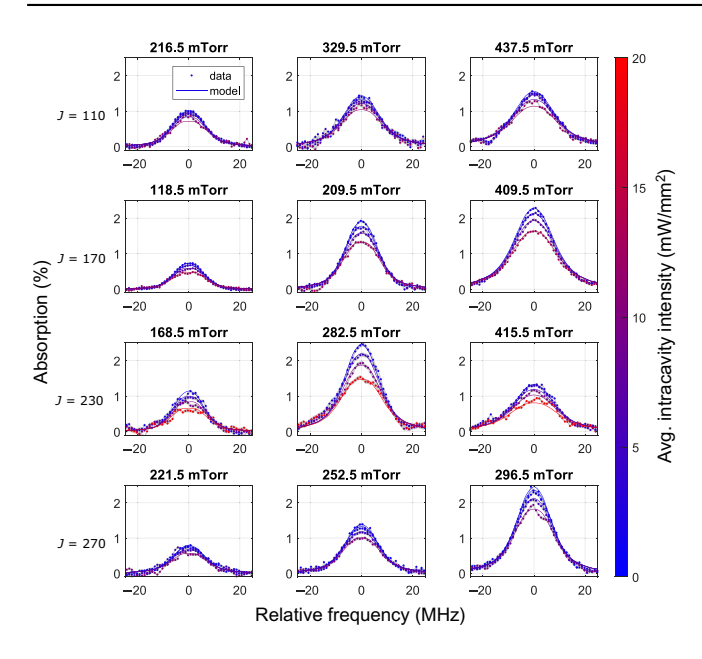


FIG. 9. Full suite of J-dependent R-branch data and rate equation model fits for $Ar-C_{60}$ data.

APPENDIX G: TRANSITION FREQUENCIES

We present expressions for the C_{60} transition frequencies. The spectroscopic constants $\Delta B = -1.8(1) \times 10^{-7}$ cm⁻¹ and $\Delta D = -8.9(9) \times 10^{-13}$ cm⁻¹ have been obtained from fitting to data in Ref. [2], assuming that the rotational temperature is fixed to 150 K. In the Q branch,

$$\nu_k = 1185 \text{ cm}^{-1} + \Delta B J_k'' (J_k'' + 1) - \Delta D (J_k'' (J_k'' + 1))^2.$$
(G1)

In the R branch,

$$v_k = 1185 \text{ cm}^{-1} + 2B(1 - \zeta)(J_k'' + 1).$$
 (G2)

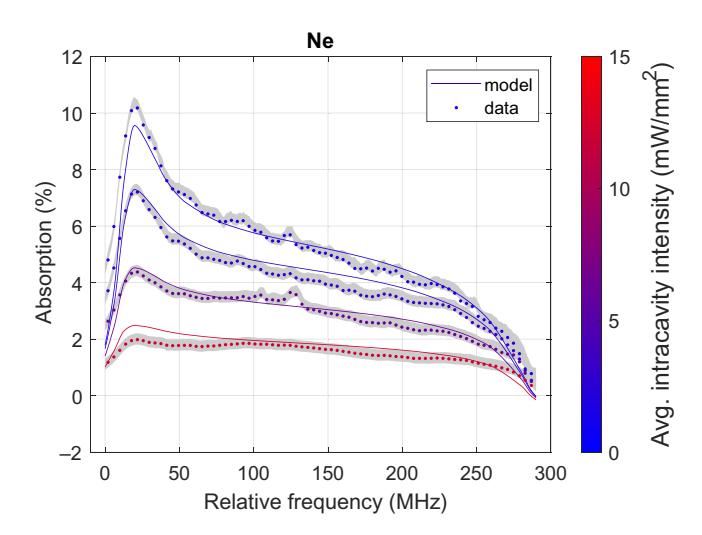


FIG. 10. Best-fit Ne-C₆₀ Q-branch profile.

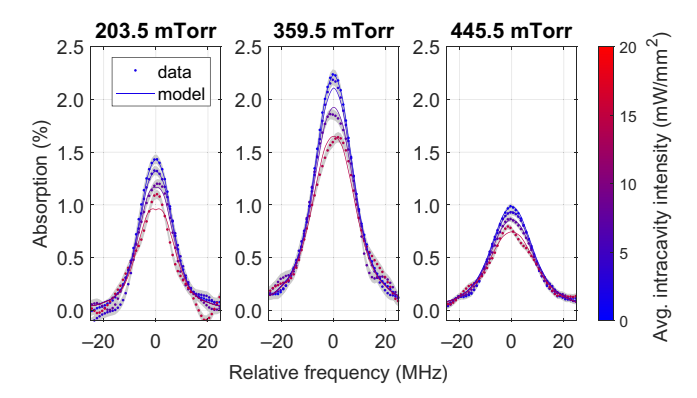


FIG. 11. Best-fit Ne-C₆₀ *R*-branch profiles.

APPENDIX H: DATA REDUCTION AND LINESHAPE FITTING FOR THE R BRANCH

To extract lineshape parameters and subtract the etalon background, we fit the raw *R*-branch data using a phenomenological lineshape function [46]:

$$f(\gamma, \sigma_D, \beta, \Delta, s_0) = Cg(\gamma, \sigma_D, \beta, \Delta)/(2\gamma'), \tag{H1}$$

$$g(\gamma, \sigma_D, \beta, \Delta) = \text{Re}\left[\frac{\Phi(z)}{1 - \sqrt{\pi}(\beta/\sqrt{2}\sigma_D)\Phi(z)}\right] / (\sqrt{2\pi}\sigma_D). \tag{H2}$$

Here

$$s = s_0 \frac{{\gamma'}^2}{\Delta^2 + {\gamma'}^2},\tag{H3}$$

$$C = \frac{\gamma'}{B(1 - [2\Delta/(A+B)]^2)^{1/2}},$$
 (H4)

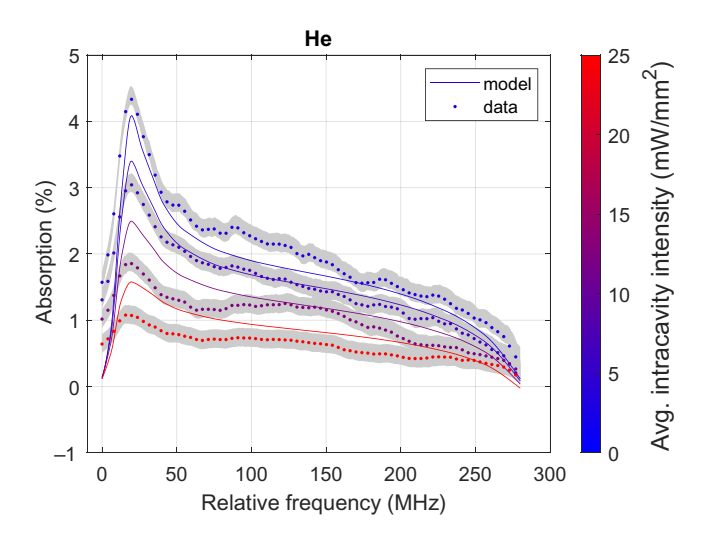


FIG. 12. Best-fit He-C₆₀ *Q*-branch profile.

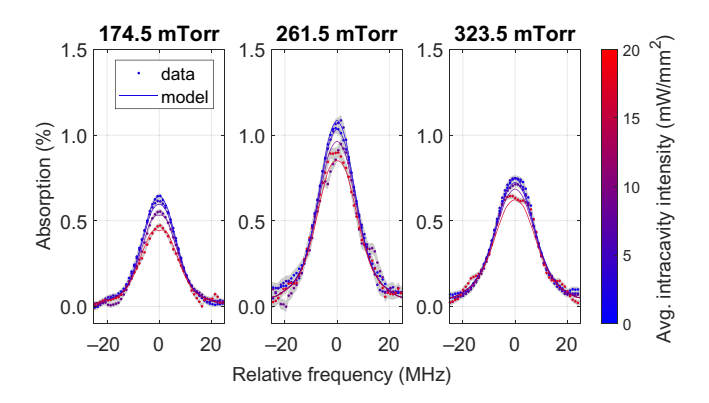


FIG. 13. Best-fit He-C₆₀ *R*-branch profiles.

$$A = (\Delta^2 + \gamma'^2)^{1/2}, (H5)$$

$$B = [\Delta^2 + \gamma'^2 (1 + 2s)]^{1/2}, \tag{H6}$$

$$\gamma' = \gamma \frac{\sqrt{1 + s_0}}{2},\tag{H7}$$

$$z = \frac{\Delta + i\gamma/2 + \beta}{\sqrt{2}\sigma_D},\tag{H8}$$

 $\Phi(z)$ is the Fadeeva function [47], and $\sigma_D = \sqrt{kT/mc^2} v_0$ is the Doppler width. We find this to perfectly reproduce saturated absorption lineshapes from the rate equation model (Appendix E) in the intermediate regime $s_0 \lesssim 1$, and $\gamma \sim \sigma_D \sqrt{8\ln(2)}$, where we operate. For C₆₀-Ar collisions, we find the best fit β , the velocity-narrowing parameter, to be consistent with zero, confirming that different velocity classes can be treated independently. For all lighter gases, we expect $\beta = 0$ to also hold at the same temperature because the momentum transferred per collision by a lighter BG must be less ($\langle \Delta p^2 \rangle = \mu kT$).

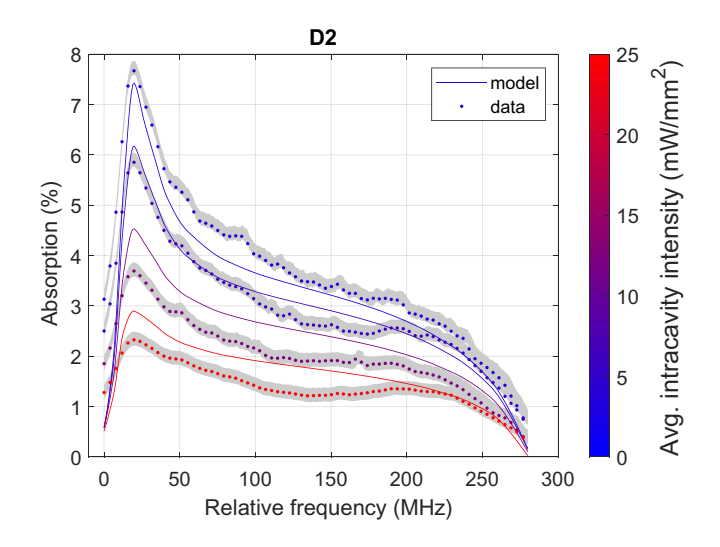


FIG. 14. Best-fit D₂-C₆₀ *Q*-branch profile.

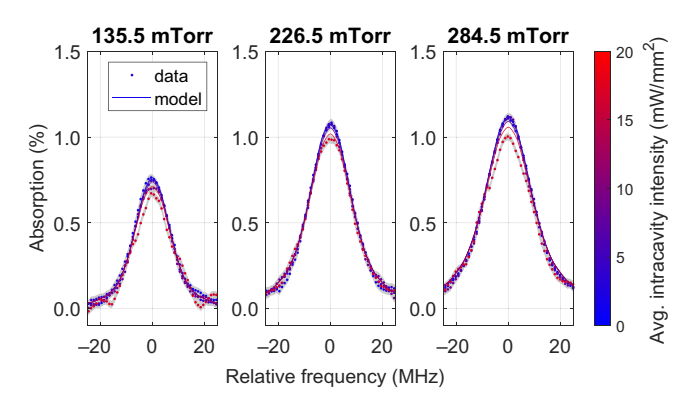


FIG. 15. Best-fit D_2 - C_{60} *R*-branch profiles.

We further constrain the relations $\gamma \equiv (1/\pi)(P/kT)\sigma_{PB}$ \overline{v}_{rel} and $s_0 = i/i_{sat}$, where $i_{sat} = \kappa + \kappa_2 \times P^2$. Fitting isolated *R*-branch saturated lineshapes taken at pressures *P* ranging from 100–400 mTorr and intensities ranging from 2–25 mW/mm² yields a set of σ_{PB} , κ , and κ_2 parameters unique to each BG species. These three parameters could then used to reproduce a family of background-free lineshapes for each BG species across arbitrary pressures and intensities for fitting to the rate equation model (Appendix E).

APPENDIX I: COMPLETE C₆₀-Ar FITTED *R*-BRANCH PROFILES

In addition to the C₆₀-Ar data shown in Figs. 2(c) and 2(d), we measure a full suite of pressure, J-dependent, and intensity-dependent R-branch absorption profiles at three pressures, at J = 110, 170, 230, and 270. The data and corresponding fits derived from the rate equation model (described in Appendix E) are shown in Fig. 9.

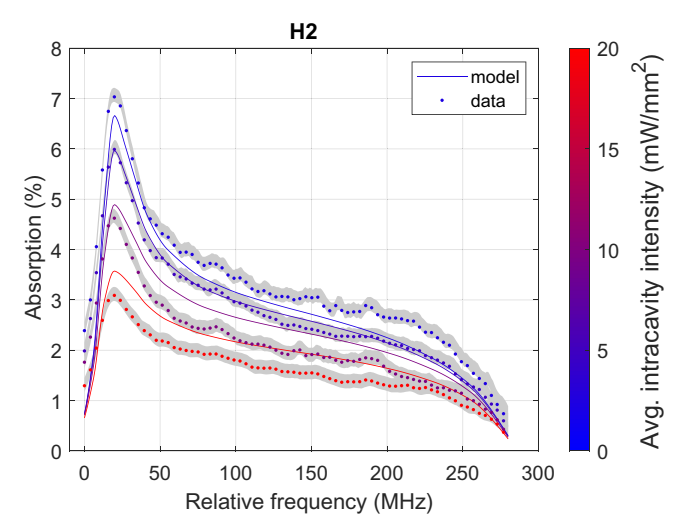


FIG. 16. Best-fit H₂-C₆₀ *Q*-branch profile.

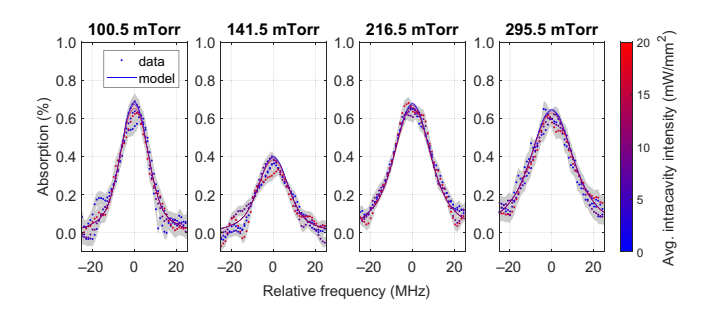


FIG. 17. Best-fit H₂-C₆₀ *R*-branch profiles.

APPENDIX J: COMPLETE C₆₀-BG FITTED PROFILES

All fitted profiles for BG = Ne, He, D_2 , and H_2 are shown in Figs. 10–17.

APPENDIX K: CALCULATING GROUND-STATE C_{60} -Ar and C_{60} -He POTENTIAL ENERGY SURFACES

The ground-state potential energy surfaces of the C_{60} -Ar and C_{60} -He complexes are not available from the literature. We therefore employ *ab initio* density functional theory (DFT) to calculate these potentials, assuming a rigid C_{60} fullerene molecule with all C atoms at their equilibrium positions as functions of the position of Ar or He. The counterpoise corrected DFT calculations are performed using the Gaussian 09 program [48], employing the hybrid wB97XD functional [49] and the 6-31G(d,p) basis set. The position of the rare-gas atom is defined in terms of coordinates (R, θ, ϕ) , where R is the separation of the noble

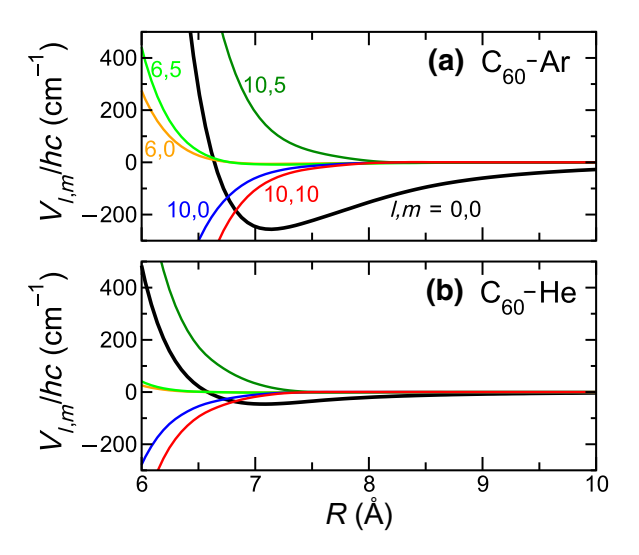


FIG. 18. Potential energy curves for C_{60} -Ar and C_{60} -He. Panels (a) and (b) show strengths $V_{l,m}(R)$ for C_{60} -Ar and C_{60} -He as functions of R, respectively. The black curves correspond to the isotropic potentials, which dominate in the atom-molecule bond. The meaning of the line colors in panels (c) and (d) is the same.

gas atom from the center of mass of C_{60} , and polar θ and azimuthal ϕ angles are defined with respect to a Cartesian coordinate system with its x and z axes along twofold and fivefold symmetry axes of C_{60} , respectively.

The rigid $^{12}C_{60}$ molecule satisfies the symmetries of the icosahedral group I_h . These symmetries restrict the allowed expansion coefficients when the potentials $V(R,\theta,\phi)$ of C_{60} -Ar and C_{60} -He are expanded in spherical harmonic functions $C_{lm}(\theta,\phi)$. In fact, we find to good approximation

$$V(R, \theta, \phi) = \sum_{l,m}^{'} V_{l,m}(R) \frac{C_{lm}(\theta, \phi) + C_{l-m}(\theta, \phi)}{2}, \quad (K1)$$

where the prime on the sum implies that $l = 0, 6, 10, 12, 16, 18, 20, m = 5n, n = 0, 1, 2, 4, and <math>0 \le m \le l$. Finally, the fitted $V_{l,m}(R)$ are potential strengths.

Panels (a) and (b) of Fig. 18 show the strongest strengths $V_{l,m}(R)$ as functions of R for Ar and He, respectively. The isotropic strength $V_{0,0}(R)$ dominates over the other coefficients for R > 7 Å. Anisotropic terms have $l, m \neq 0, 0$. The largest anisotropic contribution is that for l, m = 10, 5 followed by those for 10, 10 and 10, 0. In fact, these latter two have the opposite sign from that for l, m = 10, 5. The remaining strengths shown in the graphs are even weaker. These anisotropic strengths determine the features of inelastic collisions of C_{60} with noble gas atoms.

- [1] B. Spaun, P. B. Changala, D. Patterson, B. J. Bjork, O. H. Heckl, J. M. Doyle, and J. Ye, Continuous probing of cold complex molecules with infrared frequency comb spectroscopy, Nature 533, 517 (2016).
- [2] P. Bryan Changala, M. L. Weichman, K. F. Lee, M. E. Fermann, and J. Ye, Rovibrational quantum state resolution of the C₆₀ fullerene, Science 363, 49 (2019).
- [3] S. G. Rautian and I. I. Sobel'man, The effect of collisions on the Doppler broadening of spectral lines, Sov. Phys. Usp. 9, 701 (1967).
- [4] L. Galatry, Simultaneous effect of doppler and foreign gas broadening on spectral lines, Phys. Rev. 122, 1218 (1961).
- [5] P. L. Varghese and R. K. Hanson, Collisional narrowing effects on spectral line shapes measured at high resolution, Appl. Opt. 23, 2376 (1984).
- [6] F. Rohart, G. Wlodarczak, J. M. Colmont, G. Cazzoli, L. Dore, and C. Puzzarini, Galatry versus speed-dependent Voigt profiles for millimeter lines of O₃ in collision with N₂ and O₂, J. Mol. Spectrosc. 251, 282 (2008).
- [7] G. Nienhuis, Effects of the radiator motion in the classical and quantum mechanical theories of collisional spectral line broadening, J. Quant. Spectrosc. Radiat. Transfer 20, 275 (1978).
- [8] G. Williams, The use of the dipole correlation function in dielectric relaxation, Mol. Phys. **26**, 969 (1973).

- [9] E. W. Weber and K. Jungmann, Influence of elastic and inelastic collisions on density shift and broadening, Phys. Lett. 81, 223 (1980).
- [10] R. Ciuryło, Shapes of pressure- and Doppler-broadened spectral lines in the core and near wings, Phys. Rev. A -At. Mol. Opt. Phys. 58, 1029 (1998).
- [11] A. Schiffman and D. J. Nesbitt, Pressure broadening and collisional narrowing in $OH(v = 1 \leftarrow 0)$ rovibrational transitions with Ar, He, O_2 , and N_2 , J. Chem. Phys. **100**, 2677 (1994).
- [12] W. Demtroder, Laser Spectroscopy: Basic Concepts and Instrumentation (Springer Science and Business Media, Berlin, 2013).
- [13] J. C. Polanyi and K. B. Woodall, Mechanism of rotational relaxation, J. Chem. Phys. **56**, 1563 (1972).
- [14] R. B. Bernstein, Note on the Polanyi-Woodall equation for rotational relaxation, J. Chem. Phys. 62, 4570 (1974).
- [15] K. P. Lawley, Advances in Chemical Physics, Vol. L, Nature 16, 140 (1877).
- [16] P. R. Bunker and P. Jensen, Spherical top molecules and the molecular symmetry group, Mol. Phys.: Int. J. Interface Between Chem. Phys. **97**, 255 (1999).
- [17] M. Baranger, General impact theory of pressure broadening, Phys. Rev. 112, 855 (1958).
- [18] J. Menendez and J. B. Page, Vibrational spectroscopy of C₆₀, J. Mol. Spectrosc. 173, 431 (1995).
- [19] D. c. Tardy, B. S. Rabinovitch, and G. Z. Whitten, vibration-rotation energy-level density calculations, J. Chem. Phys 48, 1427 (1968).
- [20] R. K. Preston and R. T. Pack, Mechanism and rates of rotational relaxation of $CO_2(001)$ in He and Ar, J. Chem. Phys. **2**, 2823 (2008).
- [21] B. J. Feldman, Short-pulse multiline and multiband energy extraction in high-pressure CO2-laser amplifiers, IEEE J. Quantum Electron. 9, 1070 (1973).
- [22] C. A. Taatjes and S. R. Leone, Laser double-resonance mesurements of rotational relaxation rates of HF(J=13) with rare gases, H_2 , and D_2 , J. Chem. Phys. **89**, 302 (1988).
- [23] T. J. Michael, H. M. Ogden, and A. S. Mullin, Stateresolved rotational distributions and collision dynamics of CO molecules made in a tunable optical centrifuge, J. Chem. Phys. 154, 134307 (2021).
- [24] D. Rayane, R. Antoine, P. Dugourd, E. Benichou, A. R. Allouche, M. Aubert-Frécon, and M. Broyer, Polarizability of KC₆₀: Evidence for Potassium Skating on the C₆₀ Surface, Phys. Rev. Lett. 84, 1962 (2000).
- [25] J. Kłos, A. Petrov, and S. Kotochigova, Extraordinary collisional dynamics of icosahedral fullerenes C_{60} in a rare gas environment, (to be published 2022).
- [26] S. Osawa and E. Osawa, Non-rigid treatment of interactions between C₆₀ molecules, Fullerene Sci. Technol. 4, 329 (1996).
- [27] T. C. Briles, D. C. Yost, A. Cingöz, J. Ye, and T. R. Schibli, Simple piezoelectric-actuated mirror with 180 kHz servo bandwidth, Opt. Express 18, 9739 (2010).
- [28] P. Laurent, A. Clairon, and C. Breant, Frequency noise analysis of optically self-locked diode lasers, IEEE J. Quantum Electron. **25**, 1131 (1989).
- [29] G. Maisons, P. G. Carbajo, M. Carras, and D. Romanini, Optical-feedback cavity-enhanced absorption spectroscopy with a quantum cascade laser, Opt. Lett. 35, 3607 (2010).

- [30] G. Zhao, J. Tian, J. T. Hodges, and A. J. Fleisher, Frequency stabilization of a quantum cascade laser by weak resonant feedback from a Fabry–Perot cavity, Opt. Lett. **46**, 3057 (2021).
- [31] W. G. Harter and T. C. Reimer, Nuclear spin weights and gas phase spectral structure of ¹²C₆₀ and ¹³C₆₀ buckminsterfullerene, Chem. Phys. Lett. **194**, 230 (1992).
- [32] S. Iglesias-Groth, F. Cataldo, and A. Manchado, Infrared spectroscopy and integrated molar absorptivity of C₆₀ and C₇₀ fullerenes at extreme temperatures, Mon. Not. R. Astron. Soc. 413, 213 (2011).
- [33] R. K. Pathria and P. D. Beale, *Statistical Mechanics* (Oxford, Academic Press, 2011).
- [34] R. Zwanzig, Brownian Motion and Langevin Equations, Nonequilibrium Statistical Mechanics, 3 (2001).
- [35] T. W. Hodapp, C. Gerz, C. Furtlehner, C. I. Westbrook, W. D. Phillips, and J. Dalibard, Three-dimensional spatial diffusion in optical molasses, Appl. Phys. B Laser Opt. 60, 135 (1995).
- [36] H.-J. Werner *et al.*, Molpro, version 2015.1, a package of ab initio programs (2015).
- [37] Y. Shao, Z. Gan, and E. Epifanovsky *et al.*, Advances in molecular quantum chemistry contained in the Q-Chem 5.2 program package. (2015), Mol. Phys. 113, 184 (2015).
- [38] A. D. Becke, Density-functional exchange-energy approximation with correct asymptotic behavior, Phys. Rev. A 38, 3098 (1988).
- [39] J. P. Perdew, Density-functional approximation for the correlation energy of the inhomogeneous electron gas, Phys. Rev. B **33**, 8822 (1986).
- [40] A. Ballard, K. Bonin, and J. Louderback, Absolute measurement of the optical polarizability of C₆₀, J. Chem. Phys. **113**, 5732 (2000).
- [41] A. Derevianko, S. G. Porsev, and J. F. Babb, Electric dipole polarizabilities at imaginary frequencies for hydrogen, the alkali–metal, alkaline–earth, and noble gas atoms, At. Data Nucl. Data Tables **96**, 323 (2010).
- [42] K. L. Han, H. Lin, E. B. Gallogy, and W. M. Jackson, Total collision cross sections for C₆₀ scattering by Ar, Kr and Xe, Chem. Phys. Lett. **235**, 211 (1995).
- [43] F. V. O. N. Busch, Der Einfluss des Winkelauflosungsvermogens auf die Messung totaler atomarer Streuquerschnitte, Z. Phys. 193, 412 (1966).
- [44] M. S. Child, Molecular Collision Theory (Academic Press, London, 1974).
- [45] R. C. Hilborn, Einstein coefficients, cross sections, f values, dipole moments, and all that, Am. J. Phys. **50**, 982 (1982).
- [46] W. Demtroder, *Laser Spectroscopy Vol. 2* (Springer Science and Business Media, Berlin, 2008), Vol. 2.
- [47] J. Wang, P. Ehlers, I. Silander, and O. Axner, Dicke narrowing in the dispersion mode of detection and in noise-immune cavity-enhanced optical heterodyne molecular spectroscopy—theory and experimental verification, J. Opt. Soc. Am. B 28, 2390 (2011).
- [48] M. J. Frisch *et al.*, Gaussian 09, revision e.01 (2013), gaussian, Inc., Wallingford CT.
- [49] J.-D. Chai and M. Head-Gordon, Long-range corrected hybrid density functionals with damped atom—atom dispersion corrections, Phys. Chem. Chem. Phys. 10, 6615 (2008).